

Observation of Spin Hall Effect in Semimetal WTe₂

Bing Zhao^{1,2}, Dmitrii Khokhriakov², Yang Zhang³, Huixia Fu⁴, Bogdan Karpiak², Anamul Md. Hoque², Xiaoguang Xu¹, Yong Jiang¹, Binghai Yan⁴, Saroj P. Dash^{2,5,*}

¹Beijing Advanced Innovation Center for Materials Genome Engineering, School of Materials Science and Engineering, University of Science and Technology Beijing, Beijing 100083, China

²Department of Microtechnology and Nanoscience, Chalmers University of Technology, SE-41296, Göteborg, Sweden

³Max Planck Institute for Chemical Physics of Solids, 01187 Dresden, Germany

⁴Department of Condensed Matter Physics, Weizmann Institute of Science, Rehovot 7610001, Israel

⁵Graphene Center, Chalmers University of Technology, SE-41296 Göteborg, Sweden.

Discovery of two-dimensional (2D) topological semimetals has revealed the opportunities to realize several extraordinary physical phenomena in condensed matter physics. Specifically, these semimetals with strong spin-orbit coupling, novel spin texture and broken inversion symmetry are predicted to exhibit a large spin Hall effect that can efficiently convert the charge current to a spin current. Here for the first time, we report the direct experimental observation of a large and gate-controlled spin Hall and inverse spin Hall effects in a layered semimetal WTe₂ at room temperature obeying Onsager reciprocity relation. We demonstrate the creation and detection of the pure spin current generated by spin Hall phenomenon in WTe₂ by making van der Waals heterostructures with graphene, taking advantage of its long spin coherence length and a large spin transmission efficiency at the heterostructure interface. A large and gate-tunable spin Hall signal has been observed with spin Hall angle up to 0.37 and a spin Hall resistivity $\rho_{SH} = 3.29 \times 10^{-4} \Omega \cdot \text{cm}$ at room temperature which is almost one to two orders of magnitude larger than that of the conventional heavy metals. These experimental findings well supported by ab initio calculations; pave the way for utilization of gate tunable spin-orbit induced phenomena in 2D material heterostructures for spin-based device architectures.

Keywords: Weyl semimetals, Spintronics, Spin Hall effect, Inverse Spin Hall effect, Graphene, van der Waals heterostructures, Edelstein effect, 2D materials, TMDs, Spin transport, Gate-controlled.

Corresponding author: *Saroj P. Dash, Email: saroj.dash@chalmers.se

Department of Microtechnology and Nanoscience, Chalmers University of Technology, SE-41296, Göteborg, Sweden

Introduction

A strong resurgence of interest in two-dimensional (2D) transition metal dichalcogenide (TMD) is sparked with the successful preparation of materials with different properties that have the potential to revolutionize the future of electronics^{1,2}. While semiconducting TMDs brings enormous interest in transistors and optoelectronic applications³; the semimetals are predicted to host novel topological electronic states⁴⁻⁶. The recently predicted type-II Weyl semimetals⁶⁻⁸ such as WTe_2 and $MoTe_2$ show extraordinary electronic phenomena, like – a giant magnetoresistance⁹, high mobilities¹⁰, chiral anomaly¹¹ and anomalous Hall effect¹². These novel transport features indicate the existence of Weyl fermionic states, which are characterized by a tilted linear dispersion of Weyl cones and Fermi arc surface states. Due to the monopole-like Berry curvature in the momentum space, broken inversion symmetry and strong spin-orbit interaction, a unique spin texture in Weyl cones and Fermi arc surface states are predicted at low temperatures¹³⁻¹⁵.

Independent of topological Weyl features in these semimetals, trivial spin-polarized Fermi arc surface states are also shown to exist at the Fermi level between the electron and the hole pockets at room temperature¹⁶⁻²². Taking advantage of these properties, recent experiments with WTe_2 /ferromagnet bilayers showed an enhanced spin-torque arising from its broken inversion symmetry at the interface^{23,24}. Therefore, these 2D semimetals are considered to have a huge potential for ultra-low power spintronic devices²⁵ with an efficient conversion of charge-to-spin current, i.e. a large spin Hall effect at room temperature²⁶, however, it has not been yet experimentally measured.

Here, we demonstrate a large and gate tunable spin Hall effect (SHE) and inverse spin Hall effect (ISHE) in semimetal WTe_2 devices at room temperature. We electrically detect and quantify the spin Hall signals by employing a van der Waals heterostructure device of WTe_2 and graphene, taking advantage of 2D layered structures of both classes of the materials. In these experiments, we exploit the best of both the worlds, such as a large spin-to-charge conversion efficiency of WTe_2 , along with a long spin coherence length in graphene and an efficient spin transfer at the WTe_2 -graphene interface. Our detailed spin sensitive electronic measurements and theoretical calculations manifest the existence of a large and tunable spin Hall phenomena in WTe_2 – graphene 2D heterostructure devices at room temperature.

Results and Discussions

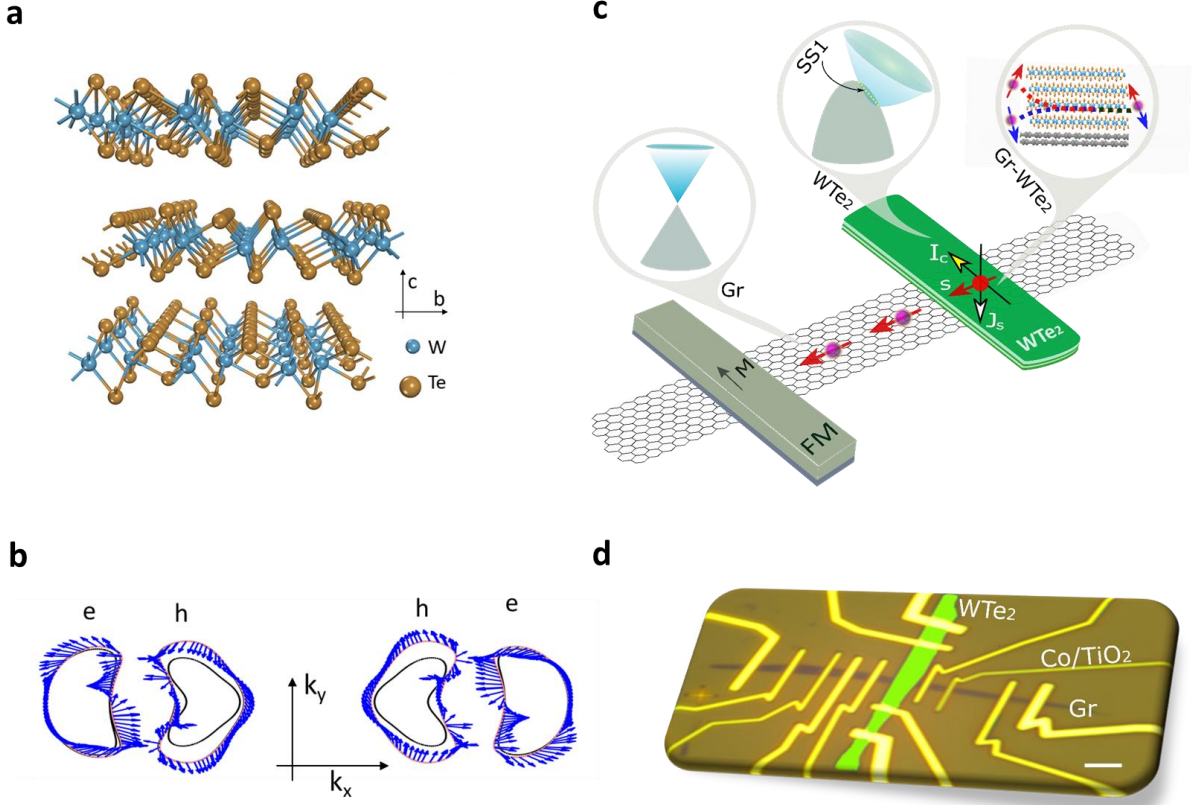


Figure 1. Scheme for detection of spin Hall and inverse spin Hall effect in WTe_2 . **a.** Crystal structure of the WTe_2 in T_d phase showing the layered nature. **b.** The calculated electronic structure showing the coexistence of both the electron (e) and hole (h) pockets on the Fermi surface. Both the electron and hole bands split into two bands (red and black). The spin texture is indicated by blue arrows in one of the split bands (red). The two split bands have opposite directions of spin polarization. **c,d.** Schematics and coloured optical microscope picture of a nanofabricated WTe_2 – graphene van der Waals heterostructure device with WTe_2 flake (green), ferromagnetic tunnel contacts of TiO_2/Co (FM) on the graphene (Gr) channel for the measurement of SHE and ISHE on a SiO_2/Si substrate. The insets in the schematics show the band structures of the materials and the structure at the interface. The scale bar (white) in the device picture is $2\mu m$.

Figures 1a and 1b show the crystal structure and calculated electronic structure, respectively, for WTe_2 in the T_d phase with the broken inversion symmetry. At the Fermi surface, small electron and hole pockets coexist, demonstrating a compensating semi-metallic feature. Because of the inversion symmetry breaking and strong SOC, each pocket splits into two bands (see Fig. 1b). The Fermi surface exhibits a clear spin texture. The left and right parts of the Fermi surface and spin texture can be transformed into each other by a mirror reflection (k_x to $-k_x$). Such as strong spin-momentum locking feature indicates that the charge current comes together with a spin current, inducing the spin Hall effect.

We experimentally investigated the influence of the spin degree of freedom on the charge currents and vis-versa due to the presence of strong spin-orbit coupling (SOC) and novel spin texture in semimetal WTe_2 . The spin Hall effect (SHE) in WTe_2 is expected to cause a transverse spin current induced by a charge current, whereas, the inverse spin Hall effect (ISHE) produces a transverse charge current that is caused by a pure spin current^{27,28}. Figure 1c,d show the nanofabricated devices consisting of van der Waals heterostructures of WTe_2 with few-layer graphene having ferromagnetic tunnel contacts to detect the SHE and ISHE in a spin sensitive potentiometric measurement (see Methods for details about the fabrication process). The heterostructure of graphene with WTe_2 flakes of 20-30 nm in thickness were used (from Hq Graphene), as measured by the atomic force microscope (AFM) (Supplementary Fig. S1). The quality of the flakes were characterized by Raman spectrometer, showing peaks corresponding to T_d -phase nature of WTe_2 (Supplementary Fig. S2).

The interface resistance between the WTe_2 and graphene was found to evolve during the measurement and finally stabilized at a very low value of $\sim 300 - 500 \Omega$ (see Supplementary Fig. S3a and Fig. S3b for Dev 1 and Dev 2 respectively). The spin transport properties of graphene channel in a heterostructure with WTe_2 are characterized by performing standard non-local spin-valve and Hanle spin precession measurements (see Fig.2a-c and Supplementary Fig. S4). The interface resistance of WTe_2 -graphene controls the spin absorption process in the heterostructure^{29,30}. As shown in Fig. 2b, an 81.3% reduction was observed in the spin-valve signal after the interface resistance reduced from 70k Ω to 300 Ω . For reference, the Hanle spin precession signals before spin-absorption process are shown in Fig. 2c for both the z- and x-magnetic field sweep directions. The efficient spin transport in graphene and strong spin absorption at the graphene- WTe_2 interface allowed the observation of both SHE and ISHE in our hybrid devices (see Supplementary Fig. S5 and Fig. S6).

Figure 2d shows the measurement geometry for spin Hall effect (SHE) and inverse spin Hall effect (ISHE) in a hybrid device consisting of WTe_2 -graphene heterostructure and a ferromagnetic contact. The contact resistance of WTe_2 -graphene in the Dev 1 during SHE measurements was around $\sim 500\Omega$ (Fig. S3a), confirming transparent interface quality. Application of a longitudinal charge current (I) in WTe_2 produces a pure transverse spin current due to SHE, which is injected into the graphene at the interface and subsequently detected as a voltage signal (V_{NL}) by the non-local ferromagnetic Co tunnel contacts after a diffusive transport in graphene. The direction of the injected spins into graphene due to SHE in WTe_2 is in-the-plane of the graphene and perpendicular to the magnetization of the ferromagnet. The magnetic field B_x is applied perpendicular to the electrodes for changing the magnetization direction of Co from 90° to 0° with respect to the injected spins. Figure 2e shows the measured SHE data of $R_{SHE} = V_{NL}/I$ for $I = 60 \mu A$ at room temperature for a B_x sweep for Dev1 with graphene channel length $L_{SHE} = 1.8 \mu m$. As expected, R_{SHE} follows a linear dependence at low B field, due to $\sin(\varphi)$ dependence of the rotation angle φ of the Co electrodes, whereas at large enough B

field, the magnetization of Co rotates 90° and become parallel to B field and also the injected spin directions, resulting in the saturation of R_{SHE} .

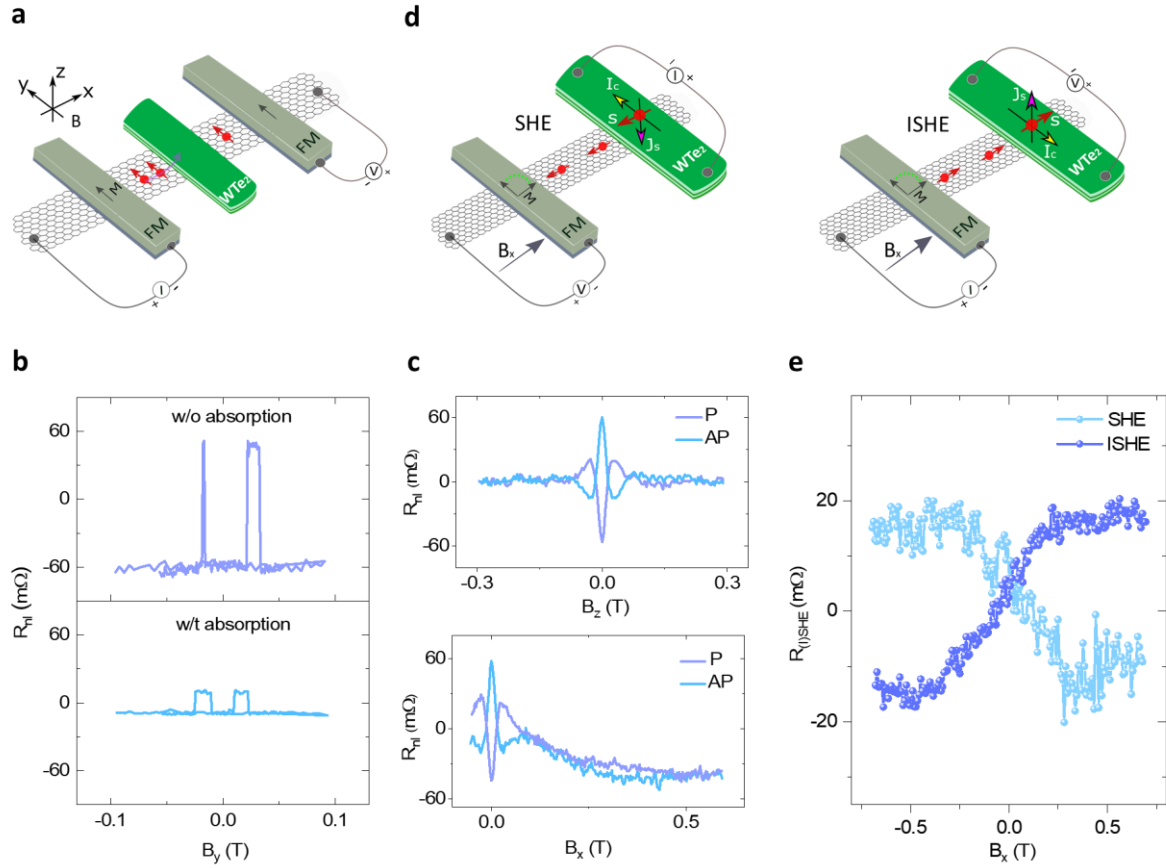


Figure 2. Electrical detection of spin Hall and inverse spin Hall effect in WTe_2 at room temperature. **a.** Schematic of the spin-valve and Hanle measurement geometry in the WTe_2 -graphene heterostructure device. **b.** The spin-valve signal measured in the graphene channel across the heterostructure with WTe_2 without spin absorption (top panel) and with spin absorption (bottom panel) as the graphene- WTe_2 interface resistance changed from 70k Ω to 300 Ω . **c.** Reference Hanle spin precession signal for different magnetic field sweep directions, B_z (upper panel) and B_x (lower panel) for both the parallel (P) and anti-parallel (AP) alignment of ferromagnetic Co electrodes. A linear background is removed from the measured spin signals. **d.** Left: Schematic diagram of spin Hall effect (SHE) measurement configuration, where a charge current in WTe_2 induces a spin current, which is injected and detected in graphene using a ferromagnetic contact in a non-local geometry, while the direction of the applied magnetic field sweep is B_x . Right: Schematic representation of inverse spin Hall effect (ISHE) measurement configuration, where a spin current injected from a ferromagnetic electrode into graphene enters the WTe_2 channel and hence induces a charge current giving rise to a voltage signal in WTe_2 , while the direction of the applied magnetic field sweep is B_x . **e.** The change in spin Hall and Inverse spin Hall resistance ($R_{(I)SHE} = V_{(I)SHE}/I$) with magnetic field B_x sweep due to the (I)SHE for bias currents of +60 μ A at room temperature for Dev 1 with channel length $L_{SHE} = 1.8 \mu$ m between Co and WTe_2 . All the measurement were performed at 300K.

Next, we performed the inverse spin Hall effect (ISHE) experiment, where a pure spin current is injected from the ferromagnet-graphene heterostructure into the WTe₂ electrode by spin absorption effect (Fig. 2d). The spin current entering the WTe₂ at the interface should give rise to a longitudinal charge voltage (V) due to the ISHE. Figure 2e shows the measured ISHE data of $R_{\text{ISHE}}=V/I$ for $I=60 \mu\text{A}$ at room temperature with $\sin \varphi$ behaviour for a B_x field sweep. These observed features confirm that the measured signal arising from spin to charge conversion in WTe₂ is due to ISHE. The opposite signs for R_{SHE} and R_{ISHE} show that the spin to charge conversion factor is positive³¹. Both the signals R_{SHE} and R_{ISHE} saturate with the magnetization of the injector/detector ferromagnetic Co electrode, as verified from the spin precession Hanle measurements with B_x field in graphene channels (see Fig. 2c and Supplementary Fig. S5). The observed similar SHE and ISHE signal magnitudes, their line shapes with magnetic field sweeps are in agreement with the Onsager reciprocity relation³² and demonstrate the generation and detection of pure spin currents in WTe₂.

The magnitude of the measured SHE and ISHE signals ($\sim 30 \text{ m}\Omega$) in WTe₂ are very large, which are two orders of magnitude larger than measured in metals (Pt) in heterostructures with Cu³³, and 3 times larger than Pt in heterostructures with graphene^{31,34}, indicating a very large spin-to-charge conversion efficiency in WTe₂. In order to quantitatively understand the SHE and ISHE data, we use a model based on one-dimensional spin diffusion equations. The detected ΔR_{ISHE} can be expressed as^{33,35,36}.

$$\Delta R_{\text{ISHE}} = \frac{2\theta_{\text{SH}}\rho_M x}{w_M} \left(\frac{\hat{I}_s}{I_c} \right) \quad (1)$$

Where the effective spin current \hat{I}_s injected vertically from graphene into the WTe₂ results in a charge current of I_c , x is the shunting factor and ρ_M , w_M and θ_{SH} are resistivity, width, spin Hall angle of WTe₂, respectively (see details in Supplementary Note 1).

We consider the spin absorption by WTe₂ across the interface, which is confirmed by non-local spin-valve experiments (see Supplementary Note 1 and Fig. S6). The spin absorption ratio \hat{I}_s/I_s is obtained to be about 51% for WTe₂-graphene interface with resistance about 300 Ω . Considering an 81.3% reduction of the spin-valve signal (Fig. 2b and Fig. S6d) and taking into consideration the graphene channel resistance and spin polarization the Co/TiO₂ contacts, the spin signal reduction due to spin absorption is consistent with the calculation of spin absorption ratio \hat{I}_s/I_s . We calculated the shunt effect factor $x \sim 0.5$ in our heterostructure (see Supplementary Note 2 and Figure S7), which is defined as the relative value under the assumption that all the charge current due to ISHE flows within WTe₂. Using these numbers, we can estimate the spin to charge current conversion efficiency, the spin Hall angle: $\theta_{\text{SH}} = \sigma_{\text{SH}}/\sigma$, where σ_{SH} and σ are the respective spin-Hall and charge conductivities of WTe₂. By numerical analysis of our experimental results, we extract the spin Hall angle $\theta_{\text{SH}} = 0.37$ and spin diffusion length $\lambda_M = 22 \text{ nm}$ in WTe₂ at room temperature (see details in Supplementary Note 2 and Fig. S7 and Fig. S8). The spin Hall conductivity of WTe₂ is estimated to be $\sigma_{\text{SH}} = 417(\hbar/e)\text{S/cm}$ for charge conductivity of $\sigma_c = 1.13 \times 10^3 \text{ S/cm}$. The corresponding spin Hall and charge resistivity of WTe₂ are $|\rho_{\text{SH}}| = 3.29 \times 10^{-4} \Omega\text{cm}$ and $\rho_c = 8.88 \times 10^{-4} \Omega\text{cm}$, respectively. In comparison to other metals reported

so far, the spin Hall resistivity of WTe_2 is one to two orders larger in magnitude compared with typical heavy metals and their alloys (see Supplement Note 3 and Fig. S9).

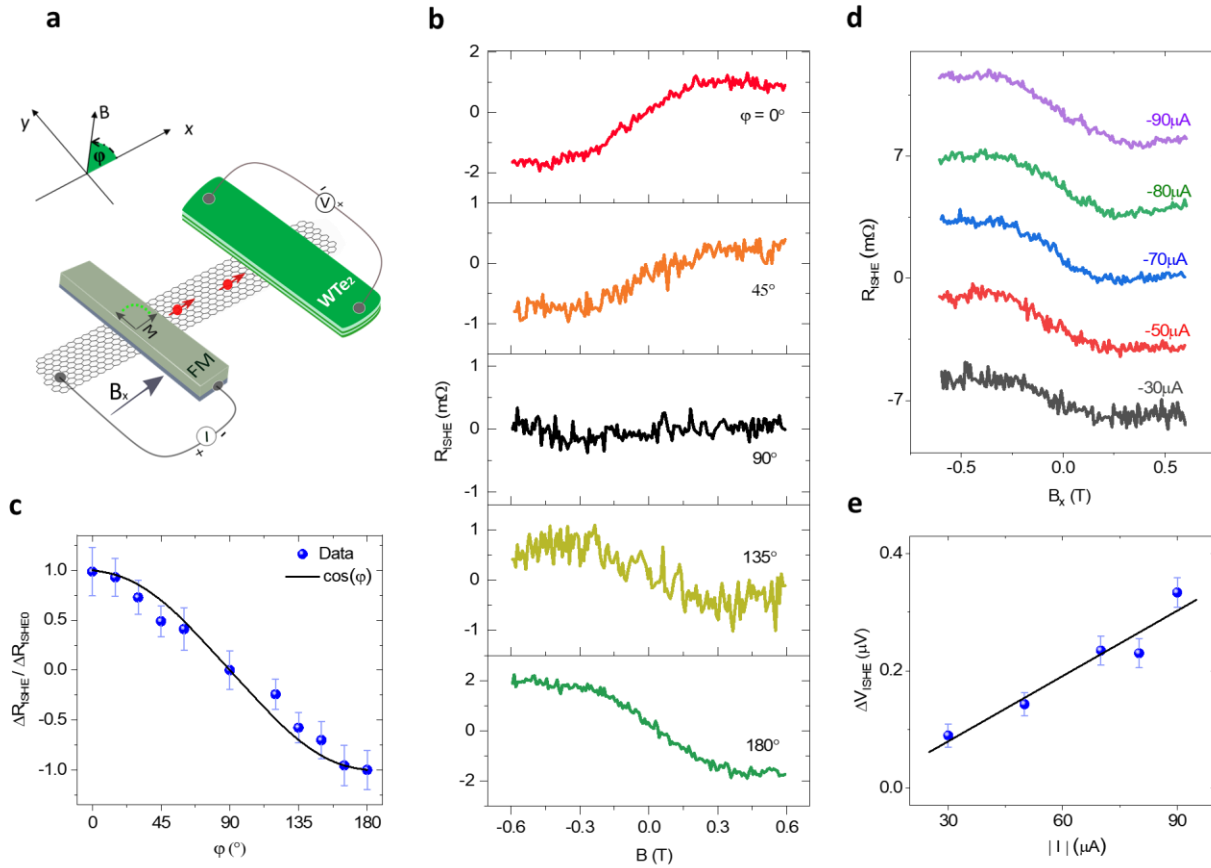


Figure 3. Angle dependence of inverse spin Hall effect in WTe_2 . **a.** Schematic representation of the ISHE measurement geometry with directions of an applied magnetic field, the detector ferromagnet magnetization and the spin current. The angle φ is defined as shown in the inset. **b.** The ISHE resistance R_{ISHE} measured at room temperature for various measurement angle orientations for Dev 2 with a graphene channel length of $L_{SHE} = 2.8 \mu\text{m}$. **c.** The normalized magnitude of ΔR_{ISHE} as a function of the direction of the magnetic field angle φ . The solid line is a $\cos(\varphi)$ curve fitted to the data points. **d,e.** The measured R_{ISHE} at different spin injection bias currents with a shift at Y axis for clarity and the magnitude of the signal with an applied bias current for the Dev 2 with channel length $L_{SHE}=2.8 \mu\text{m}$. All the measurement were performed at 300K.

The angle-dependent measurements of the inverse spin Hall signal³⁷ were performed on Dev 2 to verify the relation between the direction of the injected spins from graphene into the WTe_2 and the induced charge accumulation in WTe_2 . The measurements were carried out at different in-plane B field along the tilting angle φ from the x-axis (Fig. 3a). As shown in Fig. 3b, the measured R_{ISHE} decreases with the transverse magnetic component and vanishes when the magnetization is aligned with the y-axis. The sign change of R_{ISHE} is observed between $\varphi=0^\circ$ and $180^\circ(\pi)$ due to switching of the Co magnetization direction and associated reversal of polarization of the spin current. A null R_{ISHE} signal is observed for $\varphi = 90^\circ (\pi/2)$ when the magnetization Co is aligned with the y-axis, as the injected

spins are parallel to the magnetization of Co and no ISHE voltage is generated in the measured geometry of WTe_2 electrode. The magnitude of the measured ISHE signals R_{ISHE} as a function of the measurement angle φ is shown in Figure 3c. As expected, charge current I_c is proportional to $\mathbf{s} \times \mathbf{I}_s$ (\mathbf{s} is the spin and \mathbf{I}_s is spin current), the angular dependence of the R_{ISHE} is expected to vary with $\cos\varphi$. Such angle-dependent behaviors measured here essentially show the characteristics of inverse spin Hall effect signal³⁶, supporting spin-dependent electron scattering in WTe_2 . Figures 3d and 3e show the ISHE signal measured at different spin injection currents, and as expected ΔV_{ISHE} shows a linear behavior with bias current magnitude. The magnitude of R_{ISHE} in Dev 2 is smaller than in Dev 1 because of the longer graphene channel $L_{SHE} = 2.8 \mu m$ used here and different interface conditions.

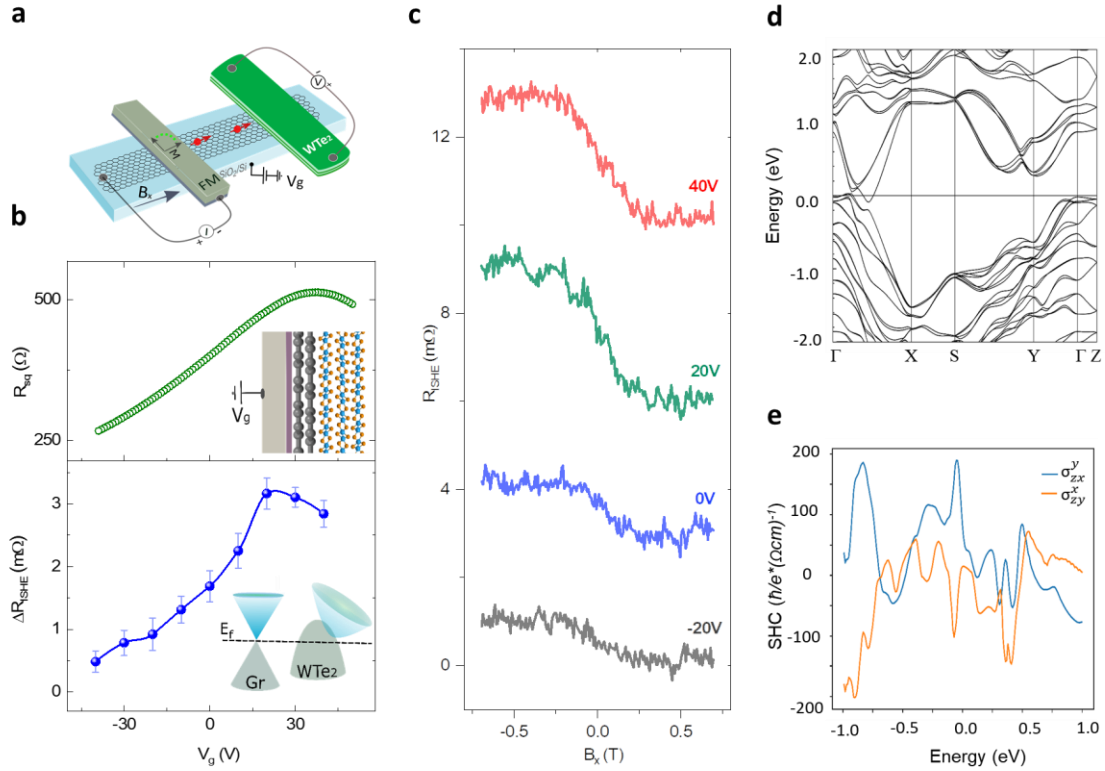


Figure 4. Gate control of spin Hall signal in the heterostructure and calculated spin Hall conductivity in WTe_2 . **a.** The ISHE measurement geometry for the gate voltage dependent measurements. **b.** Top panel: The Dirac curve of the graphene channel in the heterostructure measured in a local four-terminal measurement geometry. Bottom panel: Gate dependence of the ΔR_{ISHE} signal for Dev 2 measured in the range of $V_g = -40$ to 40 V at room temperature. The line is a guide to the eye. The insets are the schematic and band structure of graphene- WTe_2 heterostructure with an applied gate voltage (V_g). **c.** The measured spin Hall resistance R_{ISHE} at different gate voltages with a shift at Y axis for clarity. **d.** Calculated band structure of bulk WTe_2 in T_d phase with the Fermi energy is set to zero. **e.** Calculated spin Hall conductivity, σ_{zx}^y and σ_{zy}^x , with respect to the Fermi energy position in WTe_2 . All the measurement were performed at 300K.

Gate dependence of ISHE measurement was performed in WTe_2 -graphene heterostructure (Dev 2) by using the Si/SiO₂ as a back gate (Fig. 4a). The four-terminal gate voltage dependence of the resistance of graphene channel in the heterostructure shows the Dirac point at $V_D = 35$ V (Fig. 4b). The gate-

dependent measurements in WTe_2 channel resistance do not show much change due to its semi-metallic character (Fig. S3e), whereas the gate dependence of the graphene- WTe_2 interface resistance shows some modulation due to change in the graphene Fermi-energy (Fig. S3d). Figures 4b, c show the ISHE measurements and magnitude of the signal ΔR_{ISHE} at different gate voltages. Interestingly, we observe a strong increase of the signal magnitude and ΔR_{ISHE} reach a maximum as we approach the graphene Dirac point at $V_g = 30$ V. This is in contrast to the decrease of the spin signal near the graphene Dirac point V_D due to a conductivity mismatch³⁸ and also emergence of spin texture in the heterostructures³⁹. In fact, part of the enhancement in ΔR_{ISHE} can be due to increased spin absorption by WTe_2 , i.e. an increase in effective spin current \hat{I}_s injected vertically at the graphene- WTe_2 interface when the graphene resistance increase near the Dirac point^{29,30}. We also semi-quantitatively analyze the gate dependence of the ΔR_{ISHE} signal (see Supplementary note 2), which shows that the shunt effect can be tuned from 0.46 to 0.57 by the gate voltage, i.e., by changing the conductance of graphene channel. However, only these factors cannot completely explain the large enhancement observed in our experiment. Therefore, the observed gate induced enhancement in ΔR_{ISHE} can stem in parts due to contributions from spin absorption by WTe_2 or (and) the increase of charge-to-spin conversion efficiency with an electric field due to the formation of a novel spin texture at the graphene- WTe_2 interfaces⁴⁰.

The spin signal observed in our experiment can be rationalized by the bulk SHE or the Edelstein effect of the surface state in WTe_2 . In an ideal type-I Weyl semimetal (or an ideal topological insulator), in which the bulk Fermi surface vanishes, the bulk SHE is purely contributed by the topological effect. The bulk – induced spin accumulation on the surface is equivalent to that by the Edelstein effect of the topological Fermi arcs, because of the principle of the bulk-boundary correspondence⁴¹. In a type-II Weyl semimetal, in which the bulk Fermi surface always appears, the bulk SHE has both topological and Fermi surface contributions. Therefore, we should consider the bulk SHE, rather than only Fermi arcs, to include both topological effect (equivalent to surface Fermi arcs) and additional Fermi surface effect. Thus, we perform ab initio density-functional theory (DFT) calculations^{42,43} (see Methods for details) to evaluate the bulk SHE in WTe_2 . The calculated electronic band structure and spin Hall conductivity for WTe_2 are shown in Figures 4d and 4e. Here, we consider the bulk SHE that can be quantitatively estimated from the spin Berry curvature of in the band structure. The spin Hall effect refers to the generation of a spin current $J_j^i = \sigma_{jk}^i E_k$ induced by an electric field E_k , where $i, j, k = x, y, z$ (the crystallographic axes of WTe_2), and J_j^i represents a spin current along the j direction with a spin polarization along i . The spin Hall conductivity σ_{jk}^i characterizes the strength of the spin Hall effect. For a charge current along the ab plane and spin current along the c axis, we obtain corresponding intrinsic spin Hall conductivities in the range of $\sigma_{SHC} = 14 - 68 (\hbar/e)(\Omega \cdot cm)^{-1}$. Although the experimental σ_{SHC} is about six times larger, the calculated intrinsic σ_{SHC} can only

qualitatively account for the observation of significant SHE in our experiments. The extrinsic factors influencing the σ_{SHC} also required to be taken into account to quantitatively compare with the calculation results. Furthermore, as shown in Fig. 4e, the calculated spin Hall conductivity is also found to be very sensitive and depends on the position of the Fermi energy in WTe_2 . The calculated σ_{SHC} can be considerably tuned by a small change in energy, such as a tiny change in energy at 100 meV below the Fermi energy can cause a change of σ_{SHC} by nearly an order of magnitude (Fig. 4e). However, experimentally we could not tune the surface states of WTe_2 to the Fermi level by application of a gate voltage^{17,20}. As discussed earlier, the observed modulation of SHE in our experiments can be attributed to enhanced spin absorption by WTe_2 and more efficient charge-to-spin conversion at the graphene- WTe_2 interface, where the latter can be due to the formation of a novel spin texture at the graphene- WTe_2 interfaces.

Summary and Outlook

The emergent semimetal WTe_2 is shown here to be promising spin Hall materials at room temperature due to its unique electronic band structure giving rise to huge spin-orbit coupling and spin-polarized surface states. Particularly, the strong gate tunability of spin Hall signal in the WTe_2 -graphene hybrid devices provides a new tool for potential application in future spintronic device architectures. Furthermore, as predicted in theoretical calculations, the spin Hall conductivity can be controlled by using Weyl semimetals with tunable Fermi-level⁶ and alloys with tunable-resistivity. This will allow achieving systematic control over spin Hall effect via electrical and optical means and a better understanding of the Weyl physics. Such measures providing large spin Hall effect in Weyl semimetals at room temperature can be used to switch or oscillate the magnetization of nanomagnets with a very low current density. These developments will have a huge potential for emergent spin-orbit induced phenomena and applications in ultralow power magnetic random-access memory and spin logic circuits^{25,44}.

Methods

Device Fabrication - The few layers graphene were mechanically exfoliated onto the n-doped Si substrate with 300 nm SiO_2 . WTe_2 flakes were exfoliated on PDMS and dry-transferred on to the graphene flake under a microscope using a home-built micromanipulator transfer stage. Contacts to graphene and WTe_2 were defined by standard electron beam lithography and lift-off process. For the preparation of ferromagnetic tunnel contacts to graphene, a two-step deposition of 0.5 nm of Ti and oxidation process was carried out, followed by a 60 nm of Co deposition. The ferromagnetic tunnel contact (TiO_2/Co) resistances on graphene channel were in the range of few k Ω s.

Measurements - The spin Hall measurements are performed in a vacuum system equipped with a variable angular rotation facility and with an electromagnet with a magnetic field up to 0.8 Tesla. The electronics used for the measurements are Keithley 6221 current source, Keithley 2182A nanovoltmeter and Keithley 2612B source meter for application of gate voltages.

Theoretical calculation methods - We perform ab initio density-functional theory (DFT) calculations and then project the DFT wave functions to atomic-like Wannier functions with the FPLO program⁴². Based on highly

symmetric Wannier functions, we construct a tight-binding-type Hamiltonian that can fully reproduce the DFT results. Using the material-specific effective Hamiltonian, we employed the Kubo formula approach⁴³ to calculate the spin Hall conductivity.

Data availability

The data that support the findings of this study are available from the corresponding authors on reasonable request.

Acknowledgements

The authors at Chalmers University of Technology, Sweden acknowledge financial supports from EU FlagEra project (from Swedish Research council VR No. 2015-06813), Swedish Research Council VR project grants (No. 2016-03658), EU Graphene Flagship (No. 604391), Graphene center and the AoA Nano program at Chalmers University of Technology. The authors from University of Science and Technology Beijing, Beijing, China, acknowledge financial supports from the National Basic Research Program of China (Grant No. 2015CB921502) and the National Natural Science Foundation of China (Grant Nos. 51731003, 51471029). Bing Zhao would like to thank the financial support from the program of China Scholarships Council (No. 201706460036) to visit Chalmers. We thank our colleagues at the Quantum Device Physics Laboratory and Nanofabrication Laboratory at Chalmers University of Technology for their support.

Author information

Affiliations

¹ Beijing Advanced Innovation Center for Materials Genome Engineering, School of Materials Science and Engineering, University of Science and Technology Beijing, Beijing 100083, China

²Department of Microtechnology and Nanoscience, Chalmers University of Technology, SE-41296, Göteborg, Sweden

³Max Planck Institute for Chemical Physics of Solids, 01187 Dresden, Germany

⁴Department of Condensed Matter Physics, Weizmann Institute of Science, Rehovot 7610001, Israel

⁵Graphene Center, Chalmers University of Technology, SE-41296 Göteborg, Sweden.

Contributions

BZ, DK, BK and SPD fabricated and measured the devices at Chalmers University of Technology. BZ and SPD analyzed, interpreted the experimental data, compiled the figures and wrote the manuscript. DK, BK, AHM, BY, XX, YJ discussed the results and provided feedback on the manuscript. Y.Z., H.F. and B.Y. performed theoretical calculations on the band structure and spin Hall effect. SPD, YJ, BY supervised the experimental and theoretical research. SPD conceived the idea, planned the experiments and supervised the project.

Competing interests

The authors declare no competing financial interests.

Corresponding authors:

Correspondence and requests for materials should be addressed to Saroj P. Dash, Email: saroj.dash@chalmers.se

References

1. Novoselov, K. S., Mishchenko, A., Carvalho, A. & Castro Neto, A. H. 2D materials and van der Waals heterostructures. *Science (80-.)*. **353**, aac9439 (2016).
2. Manzeli, S., Ovchinnikov, D., Pasquier, D., Yazyev, O. V. & Kis, A. 2D transition metal dichalcogenides. *Nat. Rev. Mater.* **2**, 17033 (2017).
3. Wang, Q. H., Kalantar-Zadeh, K., Kis, A., Coleman, J. N. & Strano, M. S. Electronics and optoelectronics of two-dimensional transition metal dichalcogenides. *Nat. Nanotechnol.* **7**, 699–712 (2012).
4. Burkov, A. Topological semimetals. *Nat. Mater.* **15**, 1145–1148 (2016).
5. Wu, S. *et al.* Observation of the quantum spin Hall effect up to 100 kelvin in a monolayer crystal. *Science (80-.)*. **359**, 76–79 (2018).
6. Armitage, N. P., Mele, E. J. & Vishwanath, A. Weyl and Dirac semimetals in three-dimensional solids. *Rev. Mod. Phys.* **90**, 15001 (2018).
7. Zheng, H. & Zahid Hasan, M. Quasiparticle interference on type-I and type-II Weyl semimetal surfaces: a review. *Adv. Phys. X* **3**, 1466661 (2018).
8. Yan, B. & Felser, C. Topological Materials: Weyl Semimetals. *Annu. Rev. Condens. Matter Phys.* **8**, 337–354 (2017).
9. Ali, M. N. *et al.* Large, non-saturating magnetoresistance in WTe₂. *Nature* **514**, 205–208 (2014).
10. Shekhar, C. *et al.* Extremely large magnetoresistance and ultrahigh mobility in the topological Weyl semimetal candidate NbP. *Nat. Phys.* **11**, 645–649 (2015).
11. Xiong, J. *et al.* Evidence for the chiral anomaly in the Dirac semimetal Na₃Bi. **350**, 1314–1317 (2015).
12. Zhang, Y., van den Brink, J., Felser, C. & Yan, B. Electrically tuneable nonlinear anomalous Hall effect in two-dimensional transition-metal dichalcogenides WTe₂ and MoTe₂. *2D Mater.* **5**, 044001 (2018).
13. Lv, B. Q. *et al.* Observation of Fermi-Arc Spin Texture in TaAs. *Phys. Rev. Lett.* **115**, 217601 (2015).
14. Johansson, A., Henk, J. & Mertig, I. Edelstein effect in Weyl semimetals. *Phys. Rev. B* **97**, 085417 (2018).
15. Sun, Y., Wu, S.-C. & Yan, B. Topological surface states and Fermi arcs of the noncentrosymmetric Weyl semimetals TaAs, TaP, NbAs, and NbP. *Phys. Rev. B* **92**, 115428 (2015).
16. Berger, A. N. *et al.* Temperature-driven topological transition in 1T'-MoTe₂. *npj Quantum Mater.* **3**, 2 (2018).
17. Bruno, F. Y. *et al.* Observation of Large Topologically Trivial Fermi-Arcs in the Candidate Type-II Weyl Semimetal WTe₂. *Phys. Rev. B* **94**, 121112 (2016).
18. Li, P. *et al.* Evidence for topological type-II Weyl semimetal WTe₂. *Nat. Commun.* **8**, 2150 (2017).
19. Wu, Y. *et al.* Observation of Fermi arcs in the type-II Weyl semimetal candidate WTe₂. *Phys. Rev. B* **94**, 121113 (2016).
20. Wang, C. *et al.* Observation of Fermi arc and its connection with bulk states in the candidate type-II Weyl semimetal WTe₂. *Phys. Rev. B* **94**, 241119 (2016).
21. Jiang, J. *et al.* Signature of Strong Spin-Orbital Coupling in the Large Nonsaturating Magnetoresistance Material WTe₂. *Phys. Rev. Lett.* **115**, 166601 (2015).
22. Wang, Q. *et al.* Room-Temperature Nanoseconds Spin Relaxation in WTe₂ and MoTe₂ Thin Films. *Adv. Sci.* **5**, 1700912 (2018).
23. MacNeill, D. *et al.* Control of spin-orbit torques through crystal symmetry in WTe₂/ferromagnet bilayers. *Nat. Phys.* **13**, 300–305 (2017).
24. Li, P. *et al.* Spin-momentum locking and spin-orbit torques in magnetic nano-heterojunctions composed of Weyl semimetal WTe₂. *Nat. Commun.* **9**, 3990 (2018).
25. Garello, K., F. Y. *et al.* SOT-MRAM 300mm integration for low power and ultrafast embedded memories.

- arXiv Prepr. arXiv1810.10356* (2018).
26. Feng, B. *et al.* Spin texture in type-II Weyl semimetal WTe₂. *Phys. Rev. B* **94**, 195134 (2016).
 27. Sinova, J., Valenzuela, S. O., Wunderlich, J., Back, C. H. & Jungwirth, T. Spin Hall effects. *Rev. Mod. Phys.* **87**, 1213–1260 (2015).
 28. Ando, K. & Saitoh, E. Observation of the inverse spin Hall effect in silicon. *Nat. Commun.* **3**, 626–629 (2012).
 29. Dankert, A. & Dash, S. P. Electrical gate control of spin current in van der Waals heterostructures at room temperature. *Nat. Commun.* **8**, 16093 (2017).
 30. Yan, W. *et al.* A two-dimensional spin field-effect switch. *Nat. Commun.* **7**, 13372 (2016).
 31. Yan, W. *et al.* Large room temperature spin-to-charge conversion signals in a few-layer graphene/Pt lateral heterostructure. *Nat. Commun.* **8**, 661 (2017).
 32. Onsager, L. Reciprocal Relations in Irreversible Processes. I. *Phys. Rev.* **37**, 405–426 (1931).
 33. Sagasta, E. *et al.* Tuning the spin Hall effect of Pt from the moderately dirty to the superclean regime. *Phys. Rev. B* **94**, 060412 (2016).
 34. Savero Torres, W. *et al.* Spin precession and spin Hall effect in monolayer graphene/Pt nanostructures. *2D Mater.* **4**, 041008 (2017).
 35. Niimi, Y. *et al.* Extrinsic Spin Hall Effect Induced by Iridium Impurities in Copper. *Phys. Rev. Lett.* **106**, 126601 (2011).
 36. Fujiwara, K. *et al.* 5d iridium oxide as a material for spin-current detection. *Nat. Commun.* **4**, 2893 (2013).
 37. Kimura, T., Otani, Y., Sato, T., Takahashi, S. & Maekawa, S. Room-Temperature Reversible Spin Hall Effect. *Phys. Rev. Lett.* **98**, 156601 (2007).
 38. Kamalakar, M. V., Groenveld, C., Dankert, A. & Dash, S. P. Long distance spin communication in chemical vapour deposited graphene. *Nat. Commun.* **6**, 6766 (2015).
 39. Khokhriakov, D. *et al.* Tailoring emergent spin phenomena in Dirac material heterostructures. *Sci. Adv.* **4**, eaat9349 (2018).
 40. Rodriguez-Vega, M., Schwiete, G., Sinova, J. & Rossi, E. Giant Edelstein effect in topological-insulator-graphene heterostructures. *Phys. Rev. B* **96**, 235419 (2017).
 41. Essin, A. M. & Gurarie, V. Bulk-boundary correspondence of topological insulators from their respective Green's functions. *Phys. Rev. B* **84**, 125132 (2011).
 42. Eschrig, H. Full-potential nonorthogonal local-orbital minimum-basis band-structure scheme. *Phys. Rev. B - Condens. Matter Mater. Phys.* **59**, 1743–1757 (1999).
 43. Sun, Y., Zhang, Y., Felser, C. & Yan, B. Strong Intrinsic Spin Hall Effect in the TaAs Family of Weyl Semimetals. *Phys. Rev. Lett.* **117**, 146403 (2016).
 44. Soumyanarayanan, A., Reyren, N., Fert, A. & Panagopoulos, C. Emergent phenomena induced by spin-orbit coupling at surfaces and interfaces. *Nature* **539**, 509–517 (2016).

Supplementary Information

Observation of Spin Hall Effect in Semimetal WTe_2

Bing Zhao^{1,2}, Dmitrii Khokhriakov², Yang Zhang³, Huixia Fu⁴, Bogdan Karpiak², Anamul Md. Hoque², Xiaoguang Xu¹, Yong Jiang¹, Binghai Yan⁴, Saroj P. Dash^{2,5*}

¹Beijing Advanced Innovation Center for Materials Genome Engineering, School of Materials Science and Engineering, University of Science and Technology Beijing, Beijing 100083, China

²Department of Microtechnology and Nanoscience, Chalmers University of Technology, SE-41296, Göteborg, Sweden

³Max Planck Institute for Chemical Physics of Solids, 01187 Dresden, Germany

⁴Department of Condensed Matter Physics, Weizmann Institute of Science, Rehovot 7610001, Israel

⁵Graphene Center, Chalmers University of Technology, SE-41296 Göteborg, Sweden.

Corresponding author: *Saroj P. Dash, Email: saroj.dash@chalmers.se

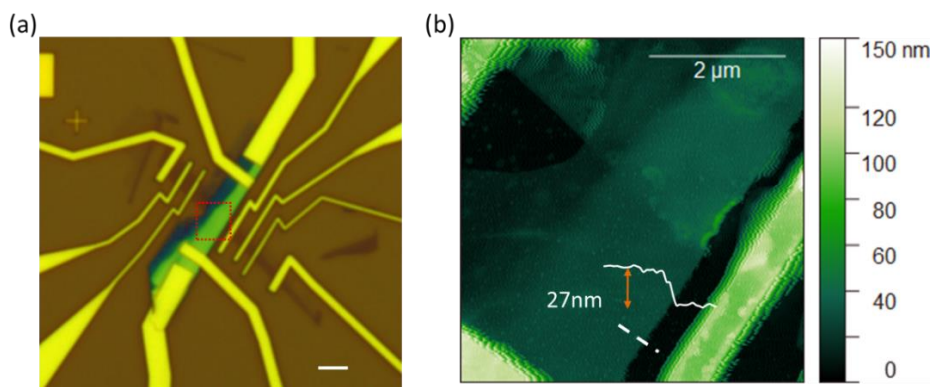


Figure S1. Device with WTe_2 -graphene heterostructure. (a) Optical micrograph of Device 1, with WTe_2 -graphene heterostructure and ferromagnetic (TiO_2 1 nm/ Co 60 nm) contacts on graphene for detection and creation of spin Hall effect (SHE) and inverse spin Hall effect (ISHE) in WTe_2 . The scale bar is 2 μm . (b) Atomic force microscope (AFM) picture of the heterostructure area (red mark in (a)). The inset shows the thickness profile of WTe_2 on graphene along the white dash line.

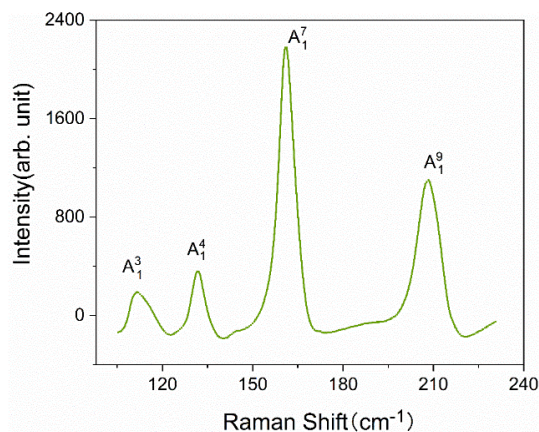


Figure S2. Raman characterization of WTe_2 . The Raman spectrum of bulk WTe_2 along c- axis using a LASER with a 638 nm wavelength. The characteristic peaks¹ located at about 112, 132, 161, and 208 cm^{-1} corresponding to the A_1^3 , A_1^4 , A_1^7 and A_1^9 , showing the T_d -phase nature of WTe_2 .

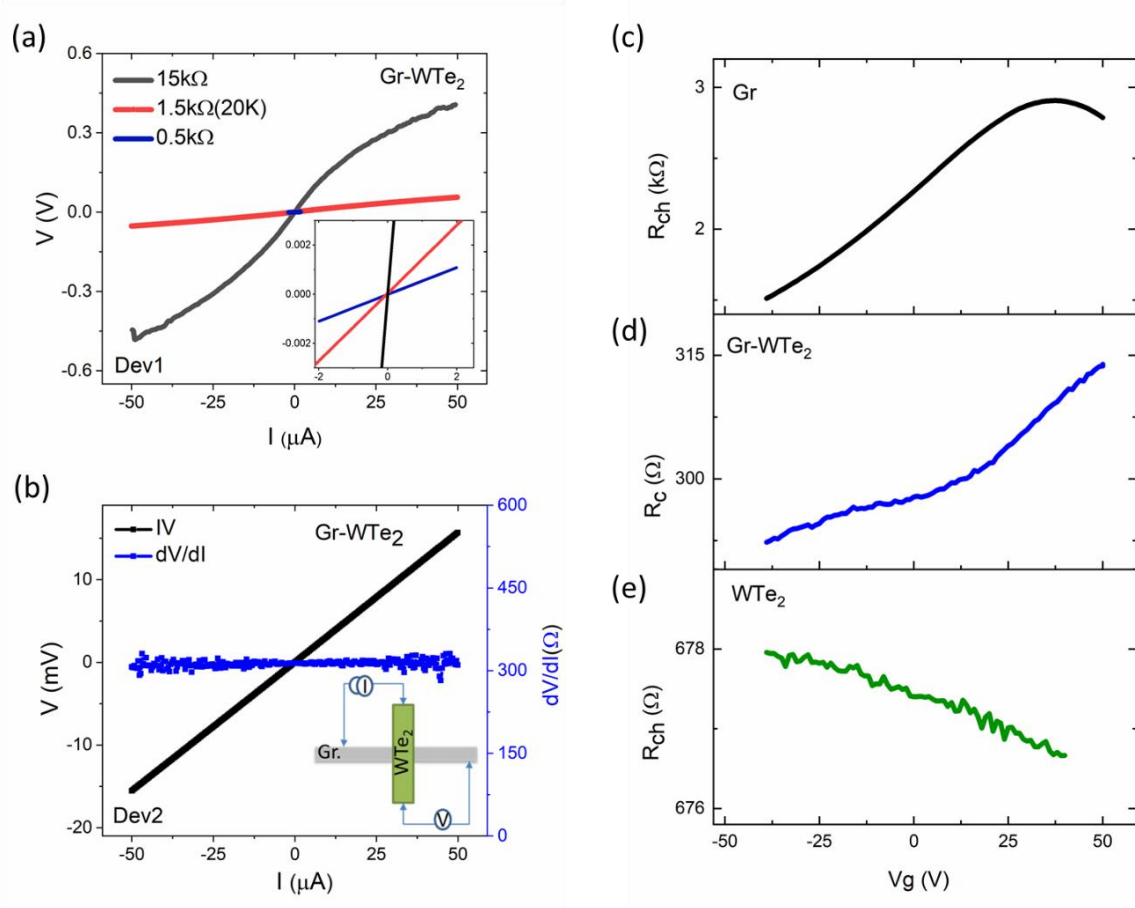


Figure S3. Electrical characterization of the graphene-WTe₂ heterostructure. (a) The current-voltage (IV) characteristics of the graphene-WTe₂ interface resistance of Dev 1 at different stages measured in a four-terminal geometry. The inset is a zoom-in part around zero bias. The interface resistance of graphene-WTe₂ is about 15 kΩ at stage-I, which is reduced to 500 Ω at stage-III. (b) The current-voltage (IV) characteristics of the graphene-WTe₂ interface resistance of Dev 2 measured in a four-terminal geometry (left axis) and corresponding differential resistance (right axis) showing about 300 Ω at stage-III. Inset is the schematic of the measurement geometry. Ultimately, both reported devices stabilized at a low contact resistance of 300-500 Ω, which is suitable for SHE and ISHE measurements. (c, d, e) Gate dependence of graphene (Gr) channel resistance, WTe₂-graphene contact resistance and WTe₂ channel resistance in Dev 2, respectively.

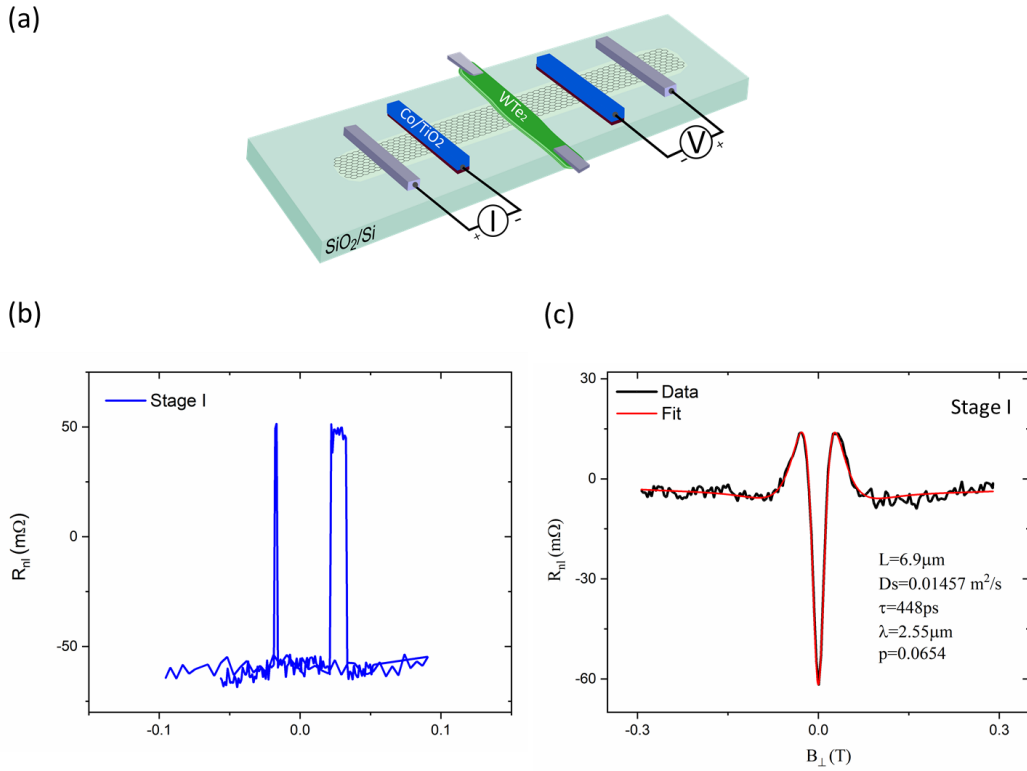


Figure S4. Spin-valve and Hanle measurements in graphene-WTe₂ heterostructures (Dev 2) in stage-I. (a) Schematics of the device and measurement geometry, where the spin signal is injected and detected by the ferromagnetic Co/TiO₂ contacts across a graphene-WTe₂ heterostructure channel. Both the spin-valve and Hanle measurements were performed in a non-local geometry by sweeping the in-plane and perpendicular magnetic fields, respectively. (b,c) Spin-valve and Hanle data in the channel at room temperature at the stage-I, when the graphene-WTe₂ interface resistance at zero-bias voltage is quite large ~ 70 k Ω . The Hanle curve data is extracted by measuring for both parallel (V_P) and anti-parallel (V_{AP}) alignment of ferromagnetic electrodes and the plot shows the data (black line) of $V_{nl}=(V_P-V_{AP})/2$. The perpendicular magnetic field is applied in the out-of-the graphene plane direction. The Hanle curve is fitted (red line) using standard spin diffusion, precession and dephasing equation². The spin parameters obtained from the fitting are noted in the inset, where L is the channel length, D_s is the diffusion constant, τ_s is the spin lifetime, λ is the spin diffusion length, p is the spin polarization of injector and detector ferromagnetic contacts.

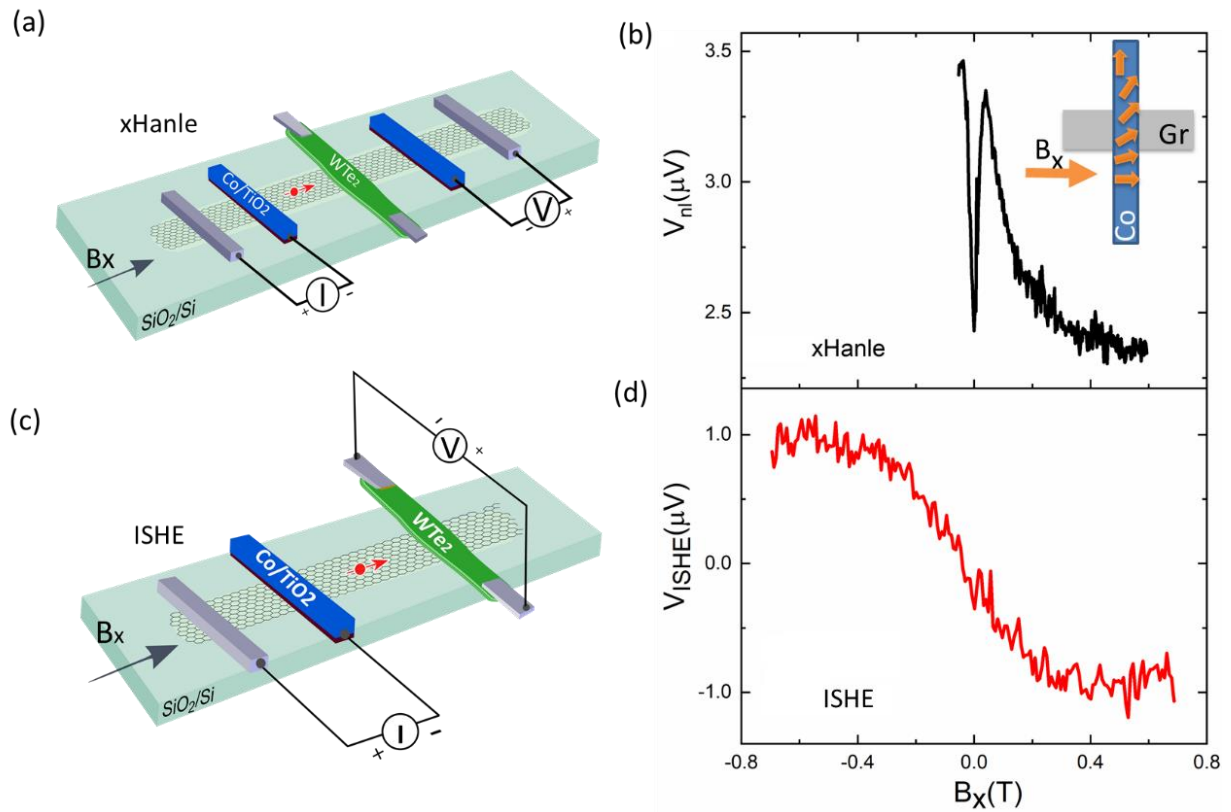


Figure S5. Estimation of magnetization saturation field from Hanle measurements. (a, b) Hanle spin precession measurement geometry and data for the graphene-WTe₂ heterostructure channel with magnetic field sweep in the direction of B_x at room temperature for Dev2 at stage-I. Inset in (b) is the schematic for the rotation of the Co magnetization when sweeping a B field in the x-direction. **(c, d)** Inverse spin Hall effect ISHE measurement geometry and data with use of same Co as spin injector contact in Dev 2. In both the Hanle and ISHE measurements the saturation magnetization is in the same B_x field range.

Note 1. Spin Absorption Effect at the Graphene-WTe₂ Interface

The spin-polarized electrons in the graphene channel can be absorbed by WTe₂ due to its high SOC, depending on the contact resistance of graphene-WTe₂ interface. We observed that the van der Waals interface contact resistance of graphene-WTe₂ usually evolved during the measurements. We distinctly observed three resistance states of the graphene-WTe₂ interface at room temperature. As shown in Fig. S6(a), stage-I shows a tunnelling type conduction, with zero-bias contact resistance (ZCR) of about 70 kΩ. Stage-II is an intermediate state with ZCR around 3kΩ (not shown in the figure). Ultimately the stage-III show a transparent interface with a very stable ZCR of 310 Ω. Similar behaviour is observed in both Dev 1 and Dev 2. Due to the decrease of the resistance and ultimate formation of transparent contact between graphene and WTe₂, the oxidation of WTe₂ at the interface can be ruled out. Such a contact behaviour is believed to be caused by a gap or air bubble at the interface introduced by our WTe₂ flake transfer method. During the fabrication process, the use of a vacuum treatment of the heterostructure before spin coating with e-beam resist, resulted in a faster evolution of the interface resistance. Moreover, the graphene channel covered by WTe₂ is found to be very stable with an almost unchanged Dirac Point (Fig. S6b), which shows a harmonious van der Waals bonding nature of graphene and WTe₂.

With the evolution of graphene-WTe₂ interface resistance, the spin current in the graphene channel gets increasingly absorbed by the WTe₂ at the interface. A direct evidence for this is the obvious decrease of the spin valve signal from 106 mΩ to 20 mΩ as the contact resistance changes from stage-I=70 kΩ to stage-III= 310 Ω (Fig. S6a and Fig. S6d). Similar behaviour is observed for graphene-WTe₂ interface resistances in both Dev 1 and Dev 2. However, the TiO₂/Co contact resistances on graphene for stage-I and -III remains comparable. Therefore, we can conclude that the strong spin absorption effect is the origin for the 81.3% reduction of the spin valve signal from state-I to stage-III, which allowed us to measure the SHE and ISHE signals in our devices. As expected, no SHE and ISHE signal could be measured for higher graphene-WTe₂ contact resistances because of very low spin absorption at the interface.

By using the Takahashi-Maekawa model³, we obtain the total spin current diffusing towards the ferromagnetic detector I_s ,

$$I_s = 2Ie^{-\frac{L}{\lambda_{gr}}} \left(\frac{p \frac{R_{c1}}{R_{gr}}}{1-p^2} \right) \left[\left(1 + 2 \frac{R_{c1}}{R_{gr}} \right) \left(1 + 2 \frac{R_{c2}}{R_{gr}} \right) e^{-\frac{2L}{\lambda_{gr}}} \right]^{-1} \quad (S1)$$

To quantitatively evaluate the spin absorption at the WTe₂-graphene interface, the ratio \hat{I}_s/I_s is calculated.

Where,

$$\begin{aligned} \frac{\hat{I}_s}{I_c} &\equiv \frac{\int_0^{t_M} I_s(z) dz}{I_c t_M} = \frac{\lambda_M (1 - e^{-\frac{t_M}{\lambda_M}})^2}{t_M (1 - e^{-2\frac{t_M}{\lambda_M}})} \frac{I_s(z=0)}{I_c} \\ &= \frac{\lambda_M (1 - e^{-\frac{t_M}{\lambda_M}})^2}{t_M (1 - e^{-2\frac{t_M}{\lambda_M}})} \frac{2pQ_{IF1} [(2Q_{IF2}+1)(1-Q_{IM})e^{-\frac{L_{SHE}}{\lambda_{gr}}} - (1+Q_{IM})e^{-\frac{3L_{SHE}}{2\lambda_{gr}}}]}{(2Q_{IF1}+1)(2Q_{IF2}+1)(1+Q_{IM}) - (2Q_{IF1}+1)(1+Q_{IM})e^{-\frac{3L_{SHE}}{2\lambda_{gr}}} - (2Q_{IF2}+1)(1-Q_{IM})e^{-\frac{L_{SHE}}{\lambda_{gr}}} - (Q_{IM}-1)e^{-\frac{2L_{SHE}}{\lambda_{gr}}}} \end{aligned} \quad (S2)$$

Where, L_{SHE} , t_M , λ_M , ρ_M , w_M and θ_{SH} are graphene channel length, WTe₂ thickness, spin diffusion length, resistivity, width, spin Hall angle of WTe₂, respectively. $R_{gr} = \frac{R_{gr} \lambda_{gr}}{w_{gr}}$, $Q_{IFi} = \frac{1}{1-p^2} \frac{R_{ci}}{R_{gr}}$, with $i=1, 2$, R_{ci}

corresponding to injector and detector contact resistance, respectively. $Q_{IM} = \frac{w_{gr}R_{cM}}{R_{gr}^2\lambda_{gr}}$, R_{cM} , w_{gr} , R_{gr} are WTe_2 -graphene interface resistance, graphene channel width and square resistance, respectively.

By substituting the experimental results, the spin absorption ratio \hat{I}_s/I_s is obtained to be about 51% for stage-III with a WTe_2 -graphene interface resistance of about 300 Ω . Considering the 81.3% reduction of the spin valve signal from stage-I to -III and taking into account the channel resistance and spin polarization Co/TiO_2 contacts, the spin signal reduction due to spin absorption is consistent with the spin absorption ratio calculation^{4,5}.

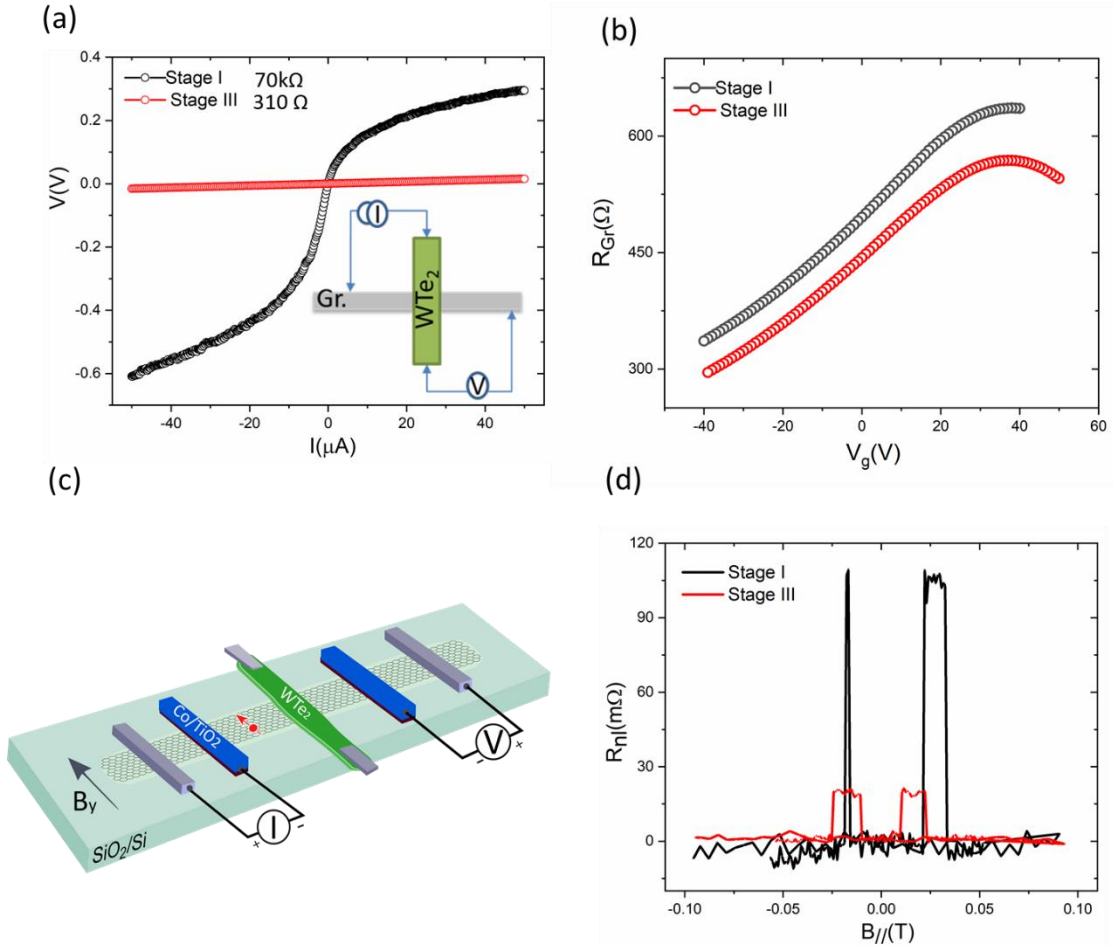


Figure S6. Spin absorption at the graphene-WTe₂ interface for Dev 2 at room temperature. (a) Current-voltage (IV) curve of the WTe₂-graphene interface contact at different stages of resistances, stage-I = 70 kΩ and stage-III = 310 Ω at room temperature. The inset shows the schematic of the four-terminal geometry used for the IV measurements. (b) Gate dependence of the square resistance of the graphene channel at these different stages. (c, d) The spin-valve measurement geometry and the signal measured in the graphene channel in the heterostructure with WTe₂. For the change of WTe₂-graphene interface contact resistances from stages-I to -III, we observed the reduction of spin signal R_{nl} from 106 mΩ to 20 mΩ at room temperature. As the injector and detector ferromagnetic contact resistances on graphene do not show any change, the reduction of the spin signal is attributed to the spin absorption at the WTe₂-graphene interface.

Note 2. Estimation of the Spin Hall Angle and Spin Diffusion Length in WTe₂

To determine the spin Hall angle, the calculation of shunt effect factor x (in Eq. 1) is very crucial^{6,7}, which is defined as the relative value under the assumption that all the charge current due to inverse spin Hall effect (ISHE) flows within WTe₂. We use COMSOL to simulate the current distribution and electric field in our WTe₂-graphene heterostructure. The model calculation is shown in Fig. S7a, with all the parameters taken from our experiments. By applying a constant current and considering the WTe₂-graphene interface resistance of 300 Ω (at stage-III), we find the shunt factor x is about 0.5. Such transparent interfaces allow the efficient spin absorption and observation of SHE and ISHE. At stage-I, where the WTe₂-graphene interface resistance is 70k Ω , the shunt effect can be highly suppressed; resulting in the absence of spin absorption and SHE and ISHE at this stage.

Additionally, our simulation results show that a further decrease of the WTe₂-graphene interface resistance does not lead to a much change of the shunt effect factor x , which means that the WTe₂-graphene interface at stage-III is transparent enough for current shunting. It is the conductance of WTe₂ and graphene that determine the shunt effect x after stage-III. The WTe₂ and WTe₂-graphene interface resistances are very weakly dependent on back gate voltage (Fig. S3d and Fig. S3e), while the conductance of graphene increases about two times (Fig. S3c), which leads to the shunt effect increasing from 0.46 to 0.57. Our calculation also shows that the shunt effect can be enhanced to 0.9 if the resistivity of graphene can be enhanced by 10 times. In practice, it is true for monolayer or few-layer graphene due to their higher electrical resistivity^{3,4}.

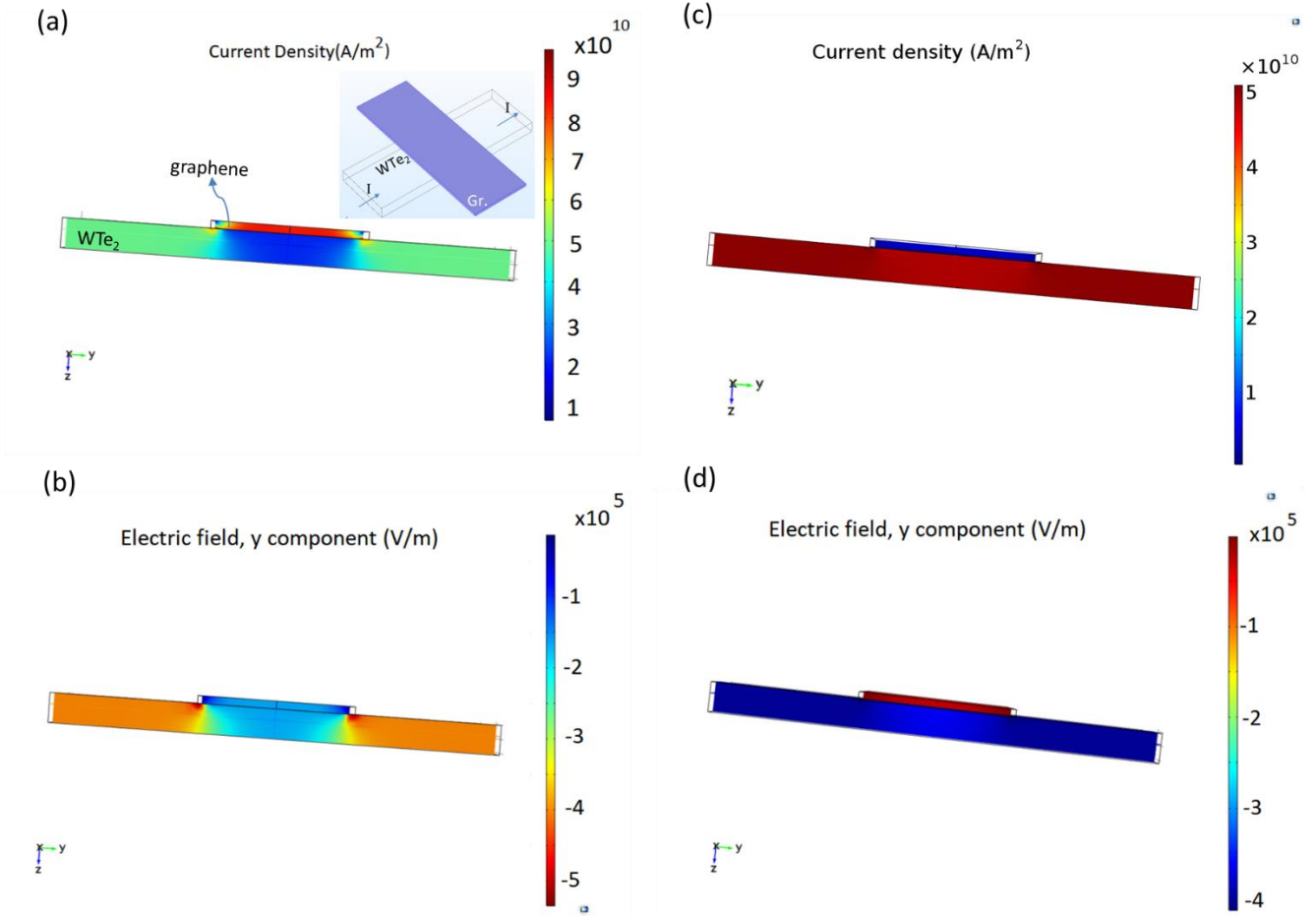


Figure S7. COMSOL simulation results of current density in WTe₂ and graphene with experimental parameters, such as WTe₂-graphene contact resistance of 300 Ω in stage-III **(a)** and 70 kΩ in stage-I **(c)**. Electrical field distribution at stage-III **(b)** and stage-I **(d)**. Insets are the schematic of the model simulation.

To estimate the spin Hall angle θ_{SH} and spin diffusion length λ_M in WTe₂, we need to consider the gate dependence of ISHE signal measured in Figure 4. As the width of WTe₂ flake is comparable to the spin diffusion length of the graphene channel, the 1D spin diffusion model to directly calculate spin diffusion length λ_M of WTe₂ is not very accurate^{8,3}. However, we still can estimate some reasonable values by numerical analysis. By solving the Eq. 1, we obtain the plot between the spin Hall angle and shunting effect $\theta_{SH} - x$, shown in Fig. S8a. We find that the solution is not sensitive to the spin diffusion length λ_M when the value is larger than 50 nm. Taking the shunt effect $x=0.5$ from our COMSOL calculation, the spin Hall angle can be 0.37, which is comparable to the largest ones obtained in heavy transition metal, like β -W⁹. In Figure S8b, we show the relation of spin Hall angle θ_{SH} with spin diffusion length λ_M for various values of the shunt factor x . From this plot, considering $\theta_{SH} = 0.37$ and $x=0.5$, we estimate the spin diffusion length λ_M at about 22 nm for WTe₂ at room temperature.

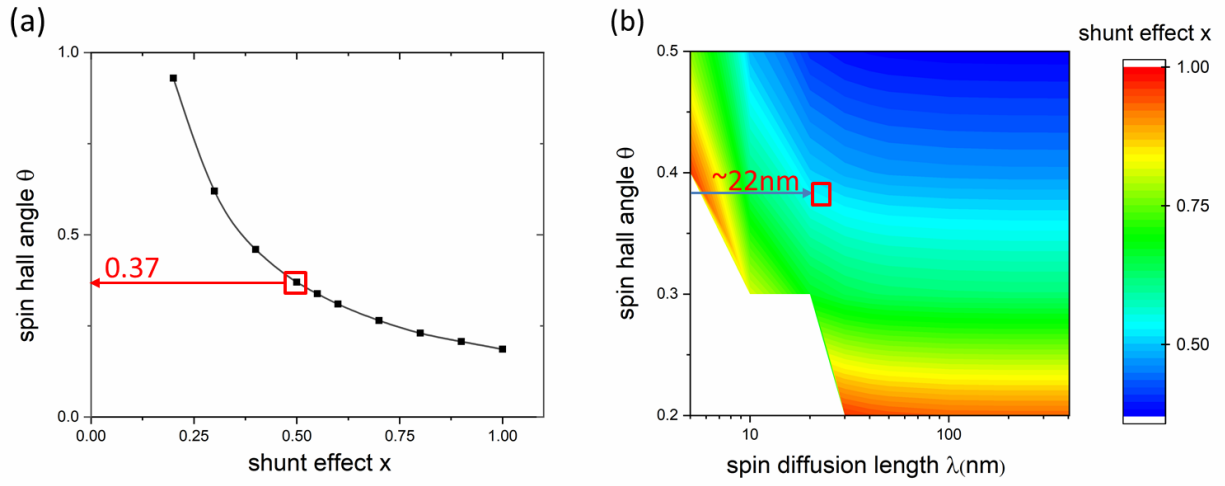


Figure S8. Estimation of spin Hall angle and spin diffusion length in WTe₂. Using a numerical solution to the Eq1 we calculate spin parameters in WTe₂. **(a)** A relation between spin Hall angle θ_{SH} and shunt effect x . For $x=0.5$, we estimate $\theta_{SH} = 0.37$. **(b)** A relation between spin Hall angle θ_{SH} and spin diffusion length λ_M for different values of the shunt effect factor x . Considering $\theta_{SH} = 0.37$ and $x=0.5$, we estimate the spin diffusion length λ_M of about 22 nm.

Note 3. Spin Hall Resistivity ρ_{SH}

The spin Hall angle is defined according to the reference¹⁰, $\theta_{SH} = -\rho_{SH}/\rho_c = \sigma_{SH}/\sigma_c$, where ρ_{SH} , ρ_c , σ_{SH} , σ_c are spin Hall resistivity, longitudinal charge resistivity, spin Hall conductivity and longitudinal charge conductivity, respectively.

Here σ_{SH} is defined in unit of \hbar/e instead of $\hbar/2e$ in other work¹¹. Correspondingly, $\sigma_{SH} = (\sigma^\uparrow - \sigma^\downarrow)/2$, where σ^\uparrow , σ^\downarrow are the real part of up spin and down spin off-diagonal conductivity component¹², respectively. Experimentally, we can obtain $|\rho_{SH}| = \theta_{SH}\rho_c = 3.29 \times 10^{-4} \Omega\text{cm}$ and $\sigma_{SH} = (\hbar/e)\theta_{SH}\sigma_c = (\hbar/e)\theta_{SH}/\rho_c = 417(\hbar/e)\text{S/cm}$. Figure S9 shows a comparison of spin Hall resistivity of WTe_2 with normal heavy metals.

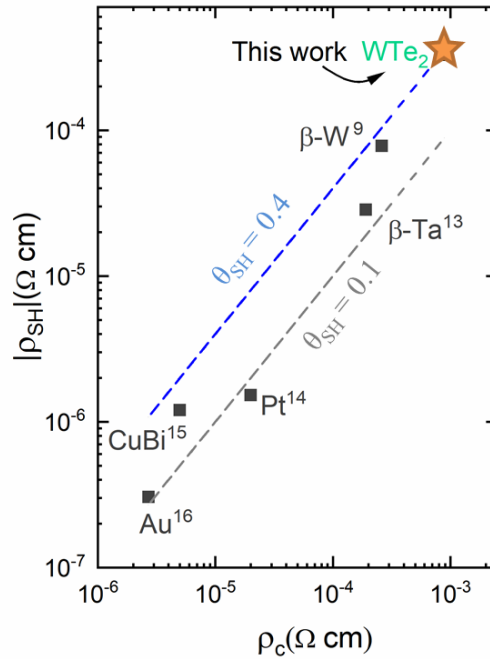


Figure S9. Experimentally measured values of spin Hall resistivity ρ_{SH} for various materials are plotted as a function of electrical resistivity ρ_c . The dash lines are the corresponding spin Hall angle guideline. In this work, spin Hall resistivity of WTe_2 $|\rho_{SH}| = 3.29 \times 10^{-4} \Omega\text{cm}$, much larger than that of normal heavy metals in other reports.

References

1. Kim, Y. *et al.* Anomalous Raman scattering and lattice dynamics in mono- and few-layer WTe₂. *Nanoscale* **8**, 2309–2316 (2016).
2. Zhao, B. *et al.* Effect of Ti doping on spin injection and relaxation in few-layer graphene. *Carbon N. Y.* **127**, 568–575 (2018).
3. Takahashi, S. & Maekawa, S. Spin injection and transport in magnetic nanostructures. *Phys. C Supercond. its Appl.* **437**, 309–313 (2006).
4. Yan, W. *et al.* Large room temperature spin-to-charge conversion signals in a few-layer graphene/Pt lateral heterostructure. *Nat. Commun.* **8**, 661 (2017).
5. Savero Torres, W. *et al.* Spin precession and spin Hall effect in monolayer graphene/Pt nanostructures. *2D Mater.* **4**, 041008 (2017).
6. Liu, L., Buhrman, R. A. & Ralph, D. C. Review and Analysis of Measurements of the Spin Hall Effect in Platinum. *arXiv Prepr. arXiv1111.3702* (2011).
7. Niimi, Y. *et al.* Extrinsic Spin Hall Effect Induced by Iridium Impurities in Copper. *Phys. Rev. Lett.* **106**, 126601 (2011).
8. Laczkowski, P. *et al.* Evaluation of spin diffusion length of AuW alloys using spin absorption experiments in the limit of large spin-orbit interactions. *Phys. Rev. B* **92**, 214405 (2015).
9. Pai, C.-F. *et al.* Spin transfer torque devices utilizing the giant spin Hall effect of tungsten. *Appl. Phys. Lett.* **101**, 122404 (2012).
10. Sagasta, E. *et al.* Unveiling the mechanisms of the spin Hall effect in Ta. *Phys. Rev. B* **98**, 060410 (2018).
11. Zhang, W. *et al.* Reduced spin-Hall effects from magnetic proximity. *Phys. Rev. B* **91**, 115316 (2015).
12. Stamm, C. *et al.* Magneto-Optical Detection of the Spin Hall Effect in Pt and W Thin Films. *Phys. Rev. Lett.* **119**, 087203 (2017).
13. Liu, L. *et al.* Spin-torque switching with the giant spin Hall effect of tantalum. *Science* **336**, 555–558 (2012).
14. Liu, L., Moriyama, T., Ralph, D. & Buhrman, R. Spin-torque ferromagnetic resonance induced by the spin Hall effect. *Phys. Rev. Lett.* **106**, 036601 (2011).
15. Niimi, Y. *et al.* Giant spin Hall effect induced by skew scattering from bismuth impurities inside thin film CuBi alloys. *Phys. Rev. Lett.* **109**, 156602 (2012).
16. Seki, T. *et al.* Giant spin Hall effect in perpendicularly spin-polarized FePt/Au devices. *Nat. Mater.* **7**, 125–129 (2008).